AIAA JOURNAL
Vol. 48, No. 3, March 2010

Experimental Investigation of Intake Ground Vortices During Takeoff

J. P. Murphy* and D. G. MacManus†
Cranfield University, Bedford, England MK43 0AL, United Kingdom
and
C. T. Sheaf‡
Rolls-Royce, Derby, England DE24 8BJ, United Kingdom

DOI: 10.2514/1.45896

A quantitative experimental investigation has been conducted to simulate intake ground vortex formation during aircraft takeoff under headwind conditions. The experiments were performed using a small-scale intake model in conjunction with a rolling ground plane in a low-speed wind tunnel. The Reynolds number was fixed at 1.26×10^6 based on the inner diameter and average intake velocity. Stereoscopic particle image velocimetry was used to measure the ground vortex velocity field, and in-duct total pressure measurements have been performed to assess the internal flow. Measurements were taken for an extensive range of configurations, including a static and simulated moving intake under a variety of headwind conditions. A moving intake was simulated in the wind tunnel by synchronizing the ground and tunnel wind velocities and using extensive suction to remove the approaching boundary layer. The results show that at high velocity ratios there are no substantial differences due to the moving ground plane. At low velocity ratios, the simulated moving intake results in a significantly different flowfield in which the ground vortex is weaker, steadier in space, and more symmetric relative to the static ground case. These results indicate the relative importance of the ground vortex vorticity sources and highlight the importance of including the effects of a moving ground when simulating an aircraft takeoff.

Nomenclature

D_i	=	intake throat diameter, m
D_l	=	highlight diameter, m
DC_{60}	=	fan face distortion coefficient based on the lowest average 60 deg sector total pressure, $(P_f - P_{60})/q_f$
h_l	=	measurement plane height from the ground plane, m
M_i	=	intake throat Mach number
P	=	local total pressure, Pa
P_f	=	area weighted fan face average total pressure, Pa
P_∞	=	freestream total pressure, Pa
P_{60}	=	minimum average 60 deg sector total pressure, Pa
q_f	=	fan face dynamic pressure, Pa
r	=	radial distance from center of vortex, m
$\bar{r}$	=	nondimensional radial distance, r/r_c
r_c	=	vortex core size, m
U_i	=	average intake velocity, m/s
U_∞	=	freestream wind velocity, m/s
u, v, w	=	velocity components in the x, y, z axis system, m/s
V_θ	=	swirl velocity, m/s
x, y, z	=	Cartesian coordinate system
Γ	=	average vortex circulation, m^2/s
Γ^*	=	average total nondimensional vortex strength, $\Gamma/D_l U_i$
δ^*	=	approaching boundary-layer displacement thickness, m
ω_z	=	out-of-plane vorticity component, 1/s

Superscripts

$+$	=	positive
$-$	=	negative

I. Introduction

WHEN an aircraft is operating in static or near-static conditions, a significant vortex can form between the ground and the intake that could potentially pose a problem to engine operation. It is well established that vortex formation can result in foreign object damage [1,2], mass flow, and total pressure distortion [3] and, therefore, premature lip flow separation [4]. It has also been recently documented that an ingested vortex can lead to fan vibration [5]. With the current design trend for turbofan configurations of increasing bypass ratio, engine diameters are also increasing and, consequently, moving nondimensionally closer to the ground plane. As a result, the likelihood of vortex formation during the aircraft operating envelope is set to increase. This is illustrated in Fig. 1, which shows the ground vortex formation boundary and vortex strength as a function of intake velocity ratio (U_i/U_∞) and engine ground height (h/D_l). With the potential for vortex formation occurring for a longer period during the takeoff run, it is therefore becoming more important to understand the characteristics and behavior of the ingested ground vortices.

Previous research has identified two fundamentally different ground vortex formation mechanisms. The first is the headwind mechanism in which vortex formation occurs due to the concentration, stretching, and intensification of ambient vortex lines associated with the dominant vorticity source [6,7]. Typically, the vorticity within the approaching boundary layer is the dominant aspect and leads to the formation of two counter-rotating vortices. The second mechanism, however, relates to an intake in a significant crosswind condition (yaw angles greater than 45 deg) in which the ground vortex is primarily generated from vorticity associated with the intake external surface [6]. Only a single vortex is generated in crosswind but it is significantly stronger than the vortices created under headwind conditions [4]. Previous to the current studies [4] there has been little quantitative knowledge of both formation mechanisms. Brix et al. [8] provides perhaps the only previous

Received 9 June 2009; accepted for publication 2 November 2009.

*Student, Department of Aerospace Sciences, School of Engineering.
†Lecturer, Department of Aerospace Sciences, School of Engineering; d.g.macmanus@cranfield.ac.uk (Corresponding Author).
‡Intake Aerodynamics Specialist, Nacelle Engineering.

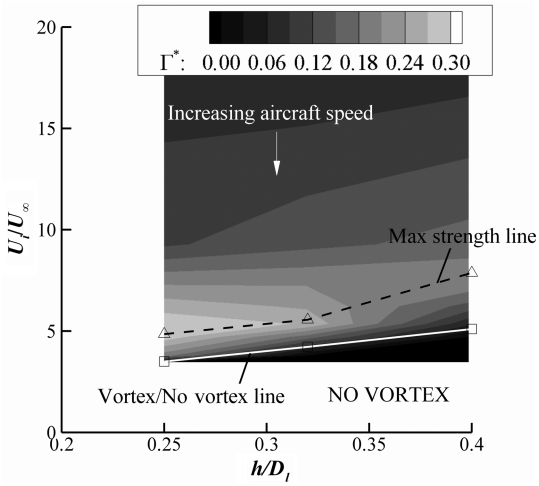

Fig. 1 Headwind vortex strength map ($\delta^*/D_l = 0.11$, $M_i = 0.58$) [4].

research containing significant quantitative information. However, this study was conducted at a single ground clearance and no distortion data were taken. In addition, only a limited range of approaching wind speeds was examined. To determine how the vortex will behave during takeoff, it is important to understand the strength and characteristics of the vortex across a range of speeds from a static condition to a speed at which the vortex no longer forms.

In a related study to the current work, Murphy [4] provided the first extensive parametric study of ground vortex formation under headwind conditions. Within this research, both external velocity and induct distortion measurements were presented with a static ground plane. The effect of both velocity ratio and ground clearance was examined, which enabled critical operating points to be quantitatively established for the first time (Fig. 1). In addition, the locus of maximum strength vortices was also established, as indicated in Fig. 1. It was shown that a vortex can form at lower than previously reported velocity ratios, which also highlights some inadequacies in much of the previous work that relied primarily on flow visualization methods only. The results from the static ground experiments will be summarized in Sec. III.

In practice, an aircraft engine is likely to experience the ground vortex ingestion for a range of conditions, such as static at the end of the runway and during taxiing, as well as during the important takeoff along the runway. To date there is no quantitative study of the ground vortex behavior for a moving aircraft. All known quantitative research has been conducted with a static ground and it is the results from such experiments that are used to interpret the vortex behavior for a moving aircraft. However, this is a significant simplification. During aircraft takeoff the headwind speed is generally constant while the aircraft accelerates down the runway. Because of the increasing aircraft speed, the indicated airspeed increases, which therefore leads to a reduction in the velocity ratio and, consequently, a reduction in the sucked stream tube size. Hence, as the velocity ratio reduces, the total ingested vorticity decreases and it is anticipated that the ground vortex circulation should decrease. This is considerably different to the static ground case in which, as the airspeed increases, the approaching ingested vorticity also increases and there is a large increase in the ground vortex strength (Fig. 1). For this reason the static ground results, such as those included in Fig. 1, are expected to lead to overly pessimistic results when applied to a moving aircraft configuration. This research therefore attempts to address this current lack of understanding and to reveal detailed information on the complex ground vortex flow mechanisms. For the first time, quantitative measurements of ground vortex formation using a rolling road to simulate forward aircraft movement are presented using stereoscopic particle image velocimetry (SPIV) and time-averaged in-duct total pressure measurements. This data set forms the last part of a large program that, to date, has explored the ground vortex characteristics under no-wind, headwind and crosswind configurations [4]. The results within this paper are compared with the previously attained static ground experiments in an increasing headwind, presented in [4], to understand the differences in the vortex boundary, strength, and formation characteristics.

II. Description of Experiments

A. Test Facility and Model

The experiments were conducted in the Cranfield University low-speed wind tunnel, which has a 2.4×1.8 m working section. A cylindrical model intake of approximately 1/30th geometric scale relative to a large-diameter modern turbofan engine was used with inside and outside diameters of 0.1 and 0.14 m, respectively. The intake Reynolds number was fixed at 1.26×10^6 based on the inner diameter and average intake velocity. Because of the low Reynolds number, transition strips were placed on both the inside and outside of the intake lip to promote transition and to avoid premature laminar separations. In addition, the lip geometry was modified relative to a

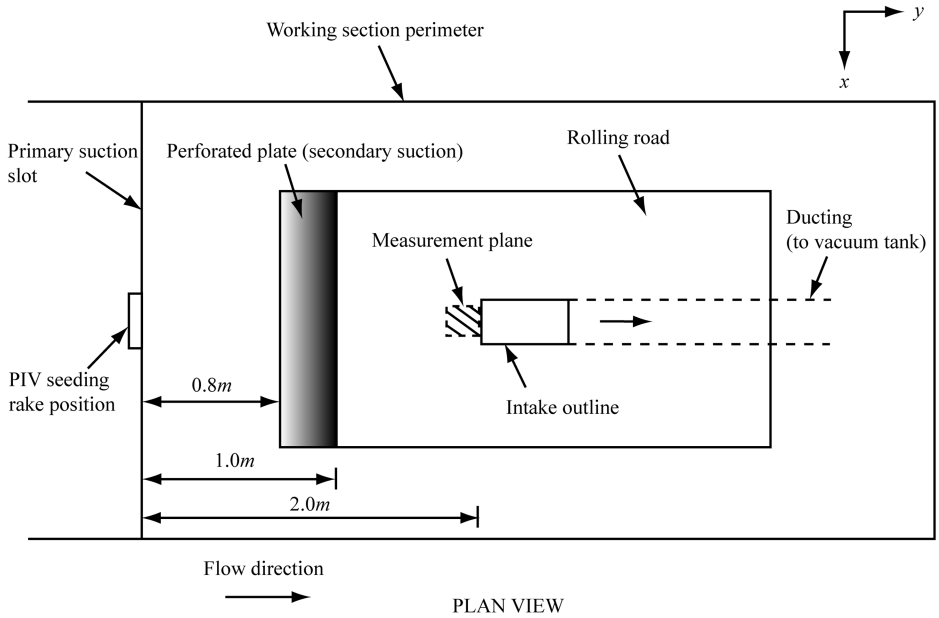

Fig. 2 Plan view schematic of tunnel working section illustrating the rolling road dimensions, intake position, and boundary suction locations (the PIV equipment has not been included for clarity).

large-scale intake and consisted of elliptical elements, with a major-to-minor axis ratio of 2. The model did not include a central hub or a rotating fan. The intake mass flow was provided by a suction system that was connected to a 60 m^3 vacuum tank. The flow was controlled using a quick release shutter valve and the required steady mass flow was achieved approximately 2 s after initiation. A run time of approximately 20 s was achieved at a constant maximum mass flow of 1.49 kg/s ($M_i = 0.58$). The mass flow was monitored for the duration of the experiments using static pressure measurements in the intake and was found to be steady throughout with a typical variation of 0.1%.

To simulate a moving aircraft over a stationary surface, a rolling ground plane was used in the wind tunnel and a schematic of the tunnel layout is shown in Fig. 2. The rolling road is 2.75 m long and 1.2 m wide. To remove any approaching boundary layer upstream of the rolling road, two substantial boundary-layer suction methods were used in the form of a slot and a perforated plate (Fig. 2). A discussion of the effectiveness of the rolling road operating in conjunction with the suction methods to removing the approaching boundary layer upstream of the intake is discussed in Sec. II.D.

B. Intake Total Pressure System

The intake was fitted with four total pressure rakes, each comprising nine total pressure probes with a head outside diameter of 1.5 mm. Total pressure measurements were taken at a location equivalent to a nominal aerodynamic interface plane $0.7D_i$ from the highlight plane. A set of 36 equispaced static pressure ports were also positioned around the inner circumference at an axial location in-line with the total pressure measurement plane. The pressure measurements were taken using a set of 40 Omega PX139-005D4V differential pressure transducers. Each pressure transducer had a range of ±5 psi with a typical repeatability of 0.1% full scale and the measurements were acquired simultaneously. For each configuration, an acquisition time of 5 s was used with a sampling frequency of 600 Hz. A total of 432 measurement points were obtained for each configuration by rotating the model around its axis (Fig. 3).

C. Particle Image Velocimetry Methodology

A TSI stereoscopic PIV system was used to acquire the three components of velocity on a plane. The PIV system consists of two 4 megapixel cameras orientated at ±45 deg to the measurement plane, with both operating in partial scatter with respect to the laser. For the static ground plane experiments, the cameras were equipped with a 60 mm focal length lens and were positioned underneath the wind-tunnel floor. For the rolling ground plane experiments, the cameras were positioned inside the tunnel working section using a 105 mm focal length lens. A New Wave Solo 120XT Nd:Yag laser with a wave length of 532 nm was used and a 1.5 mm light sheet was generated using a combination of a spherical planoconcave and a cylindrical planoconvex lenses. The position of the light sheet relative to the intake is shown in Figs. 2 and 3. The resulting flowfield snapshots were acquired at a frame rate of 7.5 Hz. The flow was seeded using a Laskin-type seeder using di-2-ethylhexyl-sebacate oil that delivered a mean particle diameter of 1 μm. The seeding rake was fixed in position for all experiments and was located upstream of the working section ahead of the wind-tunnel boundary-layer suction slots (Fig. 2).

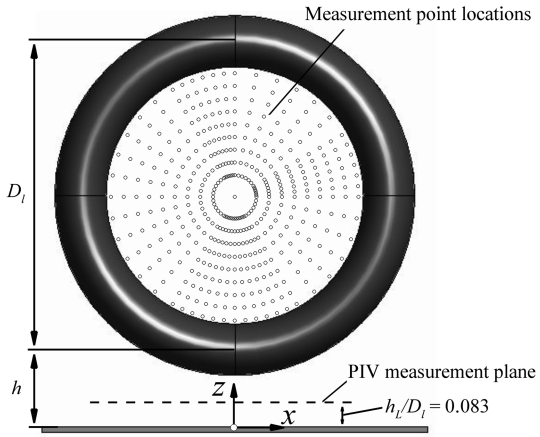

Fig. 3 Intake schematic arrangement and total pressure measurement locations within the duct.

D. Experiment Test Matrix

This investigation was primarily conducted with the intake fixed at a nondimensional height of $h/D_l = 0.25$, with a subset of measurements also taken at an h/D_l of 0.4. All experiments were performed at an intake Mach number, M_i, of 0.58. The velocity of the rolling road is denoted by U_g and can be varied from 5 to 40 m/s. The difference between the tunnel (or freestream) velocity, U_∞, and the ground speed, U_g, is given by ΔU:

$$\Delta U = U_\infty - U_g \tag{1}$$

Experiments were conducted to simulate aircraft takeoff under quiescent (no ambient wind) and headwind ambient conditions. To simulate takeoff with no ambient wind, the tunnel and ground speeds were synchronized and increased from zero while keeping ΔU constant and equal to zero (see Fig. 4b). It was impossible to simulate the aircraft acceleration; therefore, the tests were performed at a number of discrete points during the acceleration phase as defined by the velocity ratio (U_i/U_∞). The configurations examined for these synchronized rolling road cases are summarized in Table 1. This experiment is of particular interest because it aims to remove the approaching vorticity source, which has been identified as a primary vorticity source for ground vortices under headwind conditions [6]. Any approaching boundary layer developing upstream of the moving belt was removed using both the primary and secondary suction systems (Fig. 2). Ideally, for these configurations, there should be no boundary-layer growth on the rolling ground plane, but in practice it is difficult to completely remove it. Dimitriou [9] measured the boundary layer over the moving belt rig in the Cranfield University 2.4 × 1.8 m wind tunnel with the tunnel flow (U_∞) and ground speeds (U_g) synchronized at 35 m/s (i.e., $\Delta U = 0$ m/s). The boundary-layer thickness, δ, was found to be approximately 2 mm within the central portion of the road at the approximate intake highlight plane location. The vorticity flux associated with this vestigial boundary layer is at least 2 orders or magnitude smaller than the resulting ground vortex system.

To simulate an aircraft takeoff for which there is also an approaching headwind as well as the relative speed of the intake, the tunnel (U_∞) and ground (U_g) speeds are not synchronized (i.e., $\Delta U \neq 0$ m/s) (Fig. 4c). For these cases the ground speed is increased from zero, with the difference between the ground and tunnel velocity, ΔU, being kept constant. The value of ΔU represents the effective approaching headwind speed of the ambient air. Two unsynchronized configurations were investigated with ΔU equal to approximately 10 and 20 m/s, respectively (Table 2). This configuration differs from the synchronized experiments (Fig. 4b) as there is an approaching boundary layer developing on the ground upstream of the intake. But it also differs from the static ground experiments (Fig. 4a) as the wall shear stress and, hence, the approaching boundary-layer vorticity are smaller. The configurations for the unsynchronized experiments are summarized in Table 2. For this case the aim is for the approaching boundary layer to be as large as possible; therefore, no boundary-layer suction was implemented upstream of the intake. The thickness of the boundary layer in these conditions is similar to that for the static ground cases with no boundary-layer suction (i.e., $\delta^*/D_l = 0.11$). It should be noted that, given the tunnel setup, it was impossible to simulate an atmospheric boundary layer. The intention of these experiments is to examine the effect of an approaching vorticity source in conjunction with the rolling road for a single boundary-layer thickness. Nonetheless, experiments by Murphy [4] have shown that the boundary-layer thickness has little impact on the total strength of the vortex system. However, if a very large boundary layer is considered, care is

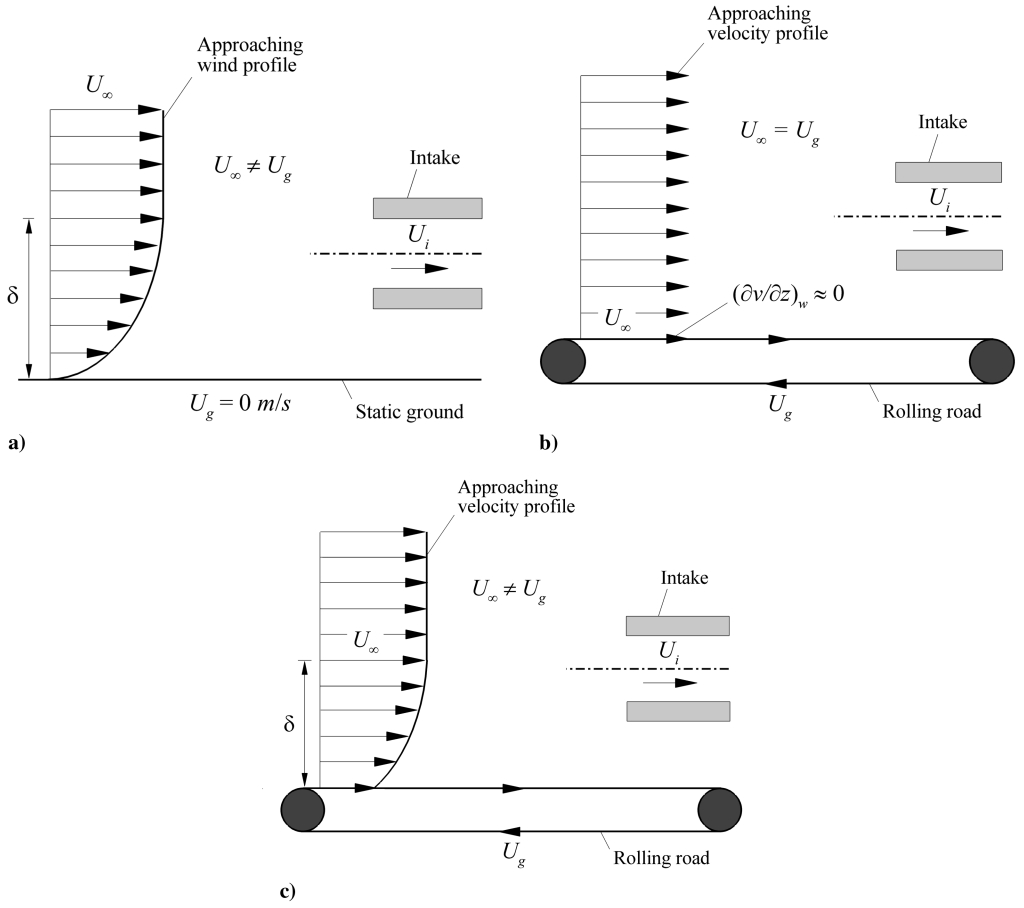

Fig. 4 Schematic of the ground arrangements: a) static ground conditions, b) synchronized ground and tunnel speeds, and c) unsynchronized ground and tunnel speeds.

required in defining the effective velocity ratio. As the sucked stream tube size is determined by the average approaching velocity within the sucked stream tube, if this is significantly different from the freestream velocity then the approaching boundary layer may have a notable impact. This is not addressed in this work.

E. Analysis Methodology

The PIV images were postprocessed using TSI Insight3G software version 8.0.5. It was found that a deformation grid, along with the fast Fourier transform (FFT) algorithm, was the best method to use for this flowfield. The method allows the procedure to be recursively implemented so that a multigrid approach can be used to further increase the signal-to-noise ratio. A 64×64 interrogation spot was used initially, with 50% overlap to maximize the correlation peak and ensure good subpixel accuracy in the displacement estimate for the windows' offsets. A pass validation was also implemented that included a median filter to remove spurious vectors and 3×3 smoothing to remove any small-scale noise present. The final iteration used a 32×32 (with 50% overlap) spot area to improve the resolution. This resulted in a measurement resolution of 0.78 mm.

Table 1 Summary of configurations investigated for the synchronized road and tunnel velocity experiments ($\Delta U \approx 0$ m/s, $M_i = 0.58$, $h/D_l = 0.25$)

Config.	U_∞, m/s	U_g, m/s	U_i/U_∞
A.1	0	0	∞
A.2	9.9	10	19.5
A.3	15.2	15	12.7
A.4	20.3	20	9.5
A.5	25.7	25	7.5
A.6	30.9	30	6.2

The position of maximum vorticity was successfully used to identify the vortex center. This parameter was preferred to more-advanced identification parameters such as the swirling strength, Q, and the eigenvalues of the velocity gradient tensor, λ_2 [10], because it can discriminate between positive and negative rotating vortices. This therefore enables such vortices to be identified and their respective characteristics to be determined individually. The vortex parameters were identified using the vorticity disk method [11]. The output of this method is a circumferentially averaged swirl velocity distribution as a function of radial distance from the center of the vortex. This method was applied by first identifying the vortex center location and then integrating vorticity over circular areas with increasing radial distance, r. The swirl velocity distribution was then obtained by dividing the local circulation at each radial position by $2\pi r$:

$$V_\theta(r) = \Gamma(r)/2\pi r \tag{2}$$

Table 2 Summary of parameters for the unsynchronized rolling road configurations ($M_i = 0.58$, $h/D_l = 0.25$)

Config.	U_∞, m/s	U_g, m/s	U_i/U_∞, m/s
	$\Delta U \approx 10$ m/s		
B.1	9.8	0	19.8
B.2	15.6	5	12.4
B.3	20.8	10	9.3
B.4	26.1	15	7.4
B.5	31.3	20	6.2
B.6	36.6	25	5.3
	$\Delta U \approx 20$ m/s		
C.1	19.1	0	10.0
C.2	26.1	5	7.4
C.3	31.2	10	6.2
C.4	36.6	15	5.3
C.5	41.9	20	4.6

The total individual vortex strength was obtained by integrating all positive vorticity over the whole circular domain for the positive vortex and vice versa for the negative vortex. The total average nondimensional strength of the vortex system, Γ^*, was then determined by averaging the vortex strengths over all snapshots, summing the magnitudes, and normalizing by the intake velocity, U_i, and highlight diameter, D_l (for further details see Murphy [4]):

$$\Gamma^* = \frac{\Gamma^+ + \Gamma^-}{U_i D_l} \tag{3}$$

F. Experiment Uncertainties

The measurement uncertainties comprise a combination of sources, such as those due to the model location, transducers, random errors, and the data acquisition system. Following the method of Taylor [12], these elements have been assessed to provide an estimate of the overall uncertainty for each measurement type.

The nondimensional height was set with an uncertainty of $h/D_l = 0.25 \pm 3.6\%$. The freestream velocity ranged from 10 to 40 m/s with a typical overall uncertainty of $\pm 1.1\%$. The average intake velocity was measured using total and static pressure measurements within the intake duct and was typically found to be 185 m/s $\pm$ 2.4%. For the duration of the run the intake velocity was reasonably constant throughout, with a typical deviation of 0.15% of the average. The velocity ratio, U_i/U_∞, ranged from ∞ to 4.6 and for a typical median velocity ratio of 6.1 the uncertainty in U_i/U_∞ was $\pm 2.6\%$. The rolling road velocity, U_g, was measured to within 0.05 m/s. Belt suction was applied throughout the testing to ensure that the rolling road did not lift or move laterally during tests.

For the PIV velocity measurements an uncertainty band was estimated following the analysis presented by Raffel et al. [13], which is based on synthetic PIV images. The analysis used an FFT correlation engine and a three-point Gaussian peak fit algorithm, which is relevant to this research. The correlation peak was estimated to be measured to within ± 0.06 pixels for each camera. Misalignment of the light sheet with the calibration plate was expected to be the largest source of error, with the center of the light sheet being, at worst, ± 0.25 mm off center. Using error estimates from Petracci et al. [14], this is expected to result in a maximum error of 0.13 pixels. The total error was expected to be no worse than ± 0.15 pixels. This equates to an in-plane velocity error of 1.61 m/s or a typical error of $\pm 3.2\%$. Because the half-angle between the cameras was at 45 deg, the out-of-plane velocity error is equal to the in-plane error in meters per second [15]. The vorticity error was therefore estimated to be approximately $\pm 1875/\text{s}$ based on the maximum velocity error. This leads to a worst-case error in the circulation of approximately ± 0.3 m^2/s. Further details on uncertainty analysis and also the experiment apparatus and procedures are presented in Murphy [4].

III. Static Ground Experiments

In this section the aerodynamics of ground vortex formation with a static ground plane (i.e., static aircraft) with an approaching headwind are summarized. The results from this section will provide a reference for the takeoff simulations presented in Sec. IV. For a more detailed discussion of the static ground headwind results, see Murphy [4].

A. Flow Topology

Under quiescent conditions ($U_\infty = 0$, $U_i/U_\infty = \infty$), a pair of contrarotating vortices form ahead of the intake highlight plane (Fig. 5a). The vortex topology is such that the right-hand vortex has a negative rotational sense. This is due to the flow being dominated by the vorticity bound in the flowfield induced by the suction between the intake and the ground. The source of vorticity for this configuration is generated by the intake-induced flowfield interacting with the ground, creating an induced boundary layer. When a small approaching headwind speed is applied, an additional source of vorticity is also introduced into the flowfield that is associated with the approaching boundary layer. With the introduction of a modest headwind ($U_\infty \approx 10$ m/s, $U_i/U_\infty = 19.8$), the flowfield immediately enters a single vortex flow mode (Fig. 5b). At this velocity ratio, ($U_i/U_\infty = 19.8$) and nondimensional height (h/D_l) of 0.25, a contrarotating vortex pair rarely forms with a positive rotating vortex prevailing for the majority of flowfield snapshots. The flowfield for this configuration is still expected to be dominated by the induced vorticity associated with the flow underneath and behind the intake highlight plane. This is indicated by the time-averaged vorticity field (Fig. 5e), for which the vorticity topology is still primarily the same as the quiescent condition case (Fig. 5d).

As the approaching wind speed increases further, the flow topology changes again with the return of a pair of contrarotating vortices (Fig. 5c). In comparison with the vortex pair generated under quiescent conditions (Fig. 5a), the vortices are stronger and with a reversed sense of rotation. This is a result of the source vorticity now being associated with the approaching flowfield [6,8].

Figure 6a shows that, with no approaching headwind, the suction-induced velocity field from the intake leads to the occurrence of two loss regions within the intake duct. This indicates the formation and ingestion of two vortices. With the introduction of a modest headwind, Fig. 6b shows that these loss cores have moved closer together; however, two regions can still be identified (Fig. 6b). As the headwind is further increased, only a single loss region can now be identified (Fig. 6c) and this pattern remains largely unchanged until the blow-away condition is reached, at which point no localized loss region is observed. Further details of these results are presented in Murphy [4] as well as in supporting computational fluid dynamics studies by Zantopp [16].

B. Vortex Strength Quantification

The effect of increasing the headwind velocity on the total average nondimensional vortex strength is presented in Fig. 7. The individual vortex strengths as well as the total nondimensional vortex circulation are shown in Fig. 7. Also included in the figure are the results from the quiescent configuration indicated by the $U_i/U_\infty = \infty$ data point. It is clear from Fig. 7 that, relative to the quiescent configuration, the introduction of a modest headwind velocity leads to no notable change in the overall vortex strength. However, the instability of the flowfield results in a change in the flow topology from a twin vortex to single vortex system that is dominated by the positive vortex element (Figs. 5 and 7). As the headwind velocity is further increased, and the velocity ratio reduced, the vortex strength increases and eventually reaches a local maximum. The two vortices are of equal strength at this point and both similarly decrease rapidly with a further reduction in velocity ratio until the blow-away condition is reached. The change in total vortex circulation with reducing velocity ratio is a result of a balance between the increase in vorticity production and the reducing sucked stream tube size. When the capture stream tube size reduces sufficiently such that it no longer interacts with the ground plane, no ground vortex forms and the strength therefore reduces to zero. The velocity ratio at which this occurs for these conditions ($h/D_l = 0.25$, $\delta^*/D_l = 0.11$) has been predicted from continuity considerations assuming a circular axisymmetric sucked stream tube and is indicated in Fig. 7 (see [4] for further details).

IV. Rolling Road Experiments

A. Synchronized Configurations ($\Delta U = 0$ m/s)

1. *Particle Image Velocimetry Velocity Flowfield*

This experiment indicates the role of the approaching boundary layer on the formation and strength of ground vortices under headwind conditions. To establish the effect of the rolling road, the experiments are compared with the static ground configurations at the same respective velocity ratios over a range of increasing headwind speeds until the vortex is no longer seen. This comparison is conducted using a series of figures that show the effect of increasing headwind speed with and without a moving ground. The metrics used to compare these configurations include snapshots of the in-plane

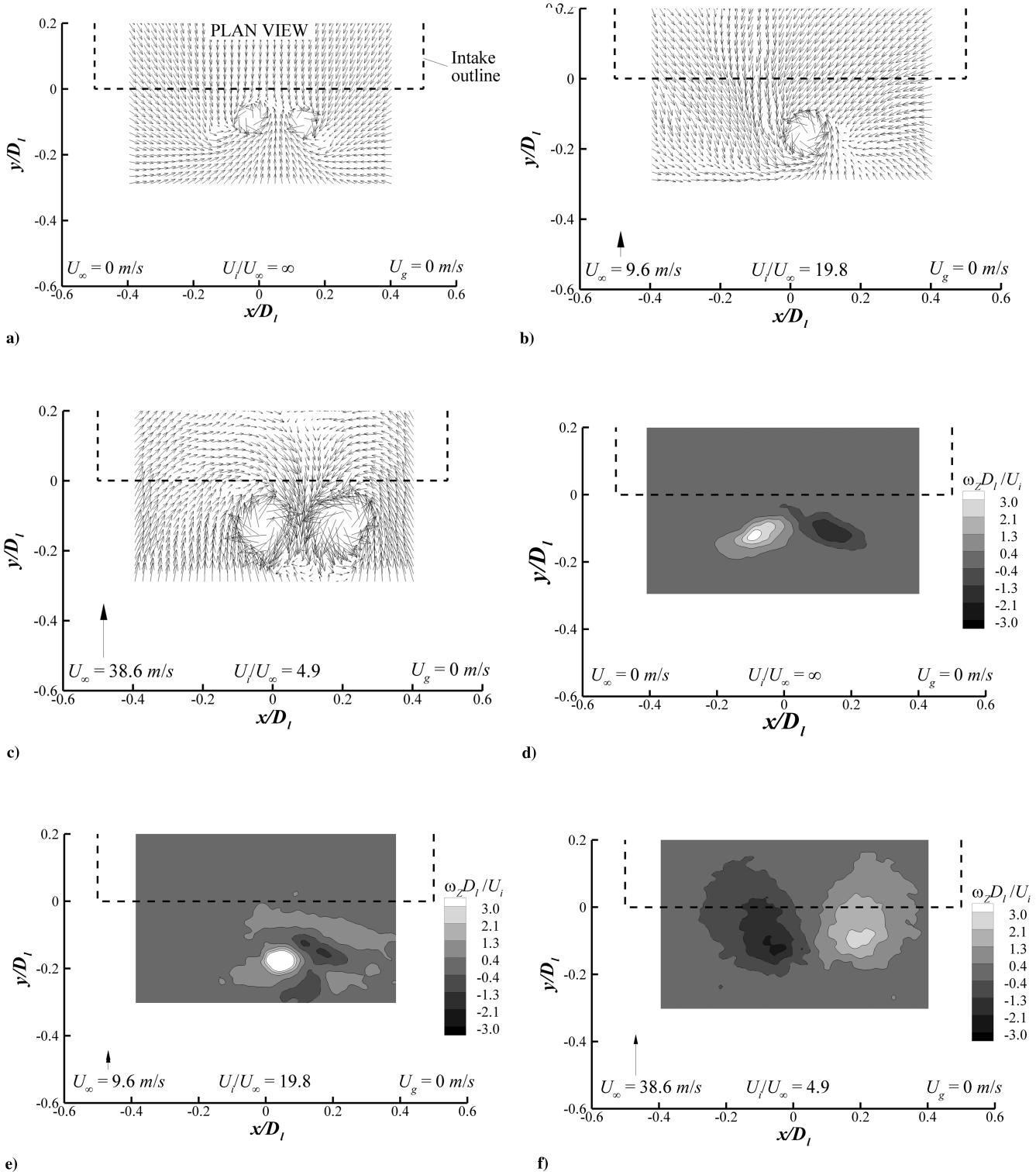

Fig. 5 Effect of increasing headwind speed from quiescent conditions over a static ground plane ($U_g = 0$ m/s): a–c) snapshots of the in-plane u–v velocity vectors (only every third vector shown), and d–f) time-averaged vorticity field ($h/D_l = 0.25$, $\delta^*/D_l = 0.11$, $M_i = 0.58$).

velocity vectors (Fig. 8) and a map of the vortex spatial unsteadiness using the locus of individual vortex core locations over all flowfield snapshots (Fig. 9), as well as the 2-D in-plane limiting streamlines of the time-averaged flowfield (Fig. 10). The ensuing discussion uses all three sets of figures to describe the influence of the rolling road.

At a relatively low headwind speed, U_∞, of approximately 15 m/s ($U_i/U_\infty = 13.3$) with a static ground ($U_g = 0$ m/s), only a single vortex is observed, which is approximately in line with the intake axis (Fig. 8a). The vortex generated under such conditions is relatively steady in space (Fig. 9a) and the time-averaged in-plane streamline agrees well with the individual snapshot, which shows a single anticlockwise rotating vortex (Fig. 10a). To examine the effect of ground speed, the rolling road is switched on, whereas the tunnel velocity is kept constant and its speed is set equal to the tunnel freestream velocity, U_∞ (i.e., it is synchronized with the tunnel velocity, U_∞). As explained earlier, the boundary suction is also switched on to remove any developing boundary-layer growth upstream of the moving belt. For this configuration (A.3 in Table 1, $U_i/U_\infty = 12.7$, $U_g = 15.2$), the velocity ratio remains approximately the same as the static ground case; however, there is now effectively no approaching boundary layer upstream of the intake. In theory, for this configuration the primary source of vorticity

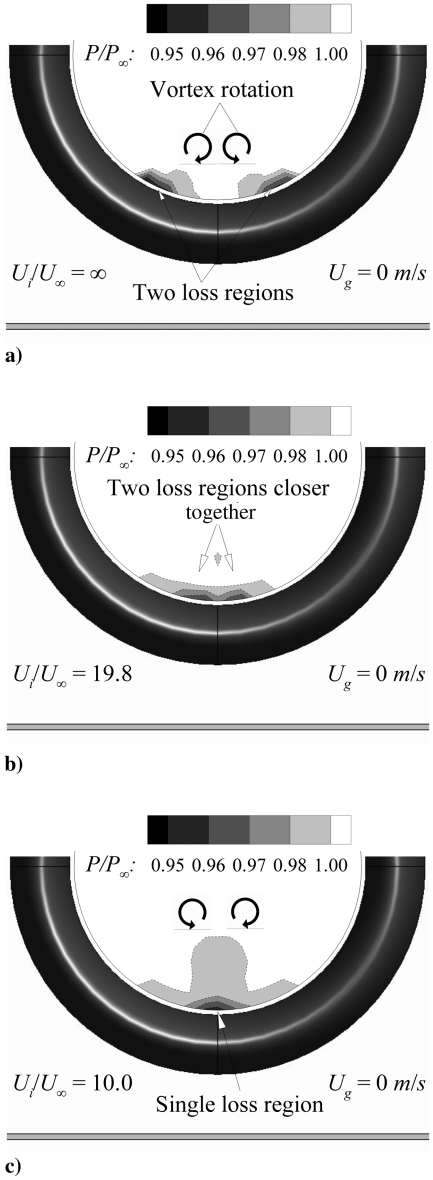

Fig. 6 Total pressure contours within the intake duct under quiescent and headwind conditions and with a static ground plane ($h/D_l = 0.25$, $U_g = 0$): a) $U_i/U_\infty = \infty$, b) $U_i/U_\infty = 19.8$, and c) $U_i/U_\infty = 10.0$.

should only be associated with the intake-induced boundary layer along the ground plane. Figure 8e displays a typical snapshot of the in-plane velocity vectors for this configuration. A single vortex can still be seen; however, in comparison to the static configuration, it is closer to the highlight plane and has an opposite sense of rotation. The change in rotation of the vortex is expected to be a result of the flowfield now being dominated by vorticity approaching the intake that has been induced by the intake suction.

In contrast to the static ground configuration, a pair of counter-rotating vortices was occasionally observed; however, a dominant vortex still exists. An examination of the sequence of flowfield snapshots reveal that when a second vortex forms its existence is short lived and is quickly engulfed by the stronger dominant vortex. This can be inferred from the locus of vortex core locations illustrated in Fig. 9e, in which there are fewer positive rotation vortices. In comparison, the prevailing vortex is very steady in space relative to both the weaker second vortex (Fig. 9e) and also the single vortex generated with a static ground plane (Fig. 9a).

The change in the flowfield structure is further illustrated by comparing the time-averaged 2-D streamlines in Figs. 10a and 10e. This shows the difference in the flowfield structure and also shows the importance of the flow emanating from underneath and behind

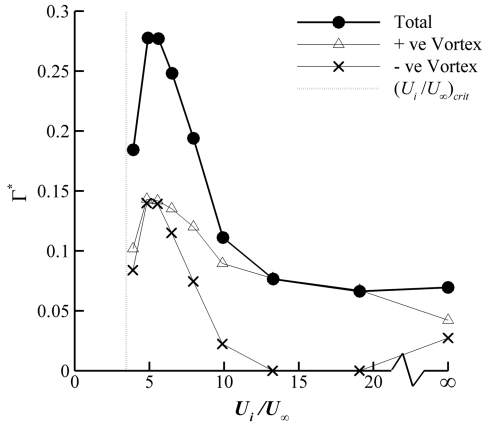

Fig. 7 Average nondimensional vortex strength against velocity ratio for a static aircraft ($U_g = 0$ m/s, $h/D_l = 0.25$, $M_i = 0.58$, $\delta^*/D_l = 0.11$).

the intake for the static ground case (Fig. 10a) in comparison with the moving ground results, which show the flowfield to be dominated by the approaching flow (Fig. 10e). It is also evident when comparing the two figures that the region of flow emanating from aft and underneath the intake is also significantly smaller for the rolling road configuration. As a consequence, the balance between the aft and approaching flowfields leads to the vortex being closer to the intake highlight plane. This feature is also expected to be due to the reduced sucked stream tube size, a result of the absence of the approaching boundary layer.

As the headwind velocity, U_∞, increases to 20 m/s, a dramatic difference is now seen between the static ground (A.4, $U_g = 0$ m/s) and the equivalent rolling road configuration (C.1, $U_g = 20$ m/s). For a static ground plane a single dominant vortex is still usually observed (Fig. 8b), with a counter-rotating vortex pair also sporadically seen that possesses the headwind rotation mode (i.e., the vortices rotate in accord with Fig. 5c). Evidence of this is presented in Fig. 9b, which shows the snapshot positions of both the positive and negative vortex cores. This figure also reveals an increase in the spatial unsteadiness of the vortex relative to the higher velocity ratio of 13.3 (Fig. 9a). In contrast, for the moving ground case, two equal strength counter-rotating vortices are consistently observed for all flowfield snapshots (Fig. 9f). The difference can be clearly seen in the time-averaged flowfield, in which a single large vortex is observed for the static ground case (Fig. 10b), whereas for the rolling road two counter-rotating vortices can be visualized (Fig. 10f). The flowfield for the moving ground configuration now has symmetry about the intake axis. This differs from the $U_g = 0$ cases in which a symmetric flowfield is never observed across the range of headwind speeds shown in Fig. 10. Finally, at a low-velocity ratio of approximately 6.6, the static ground configuration shows a still-stronger pair of contrarotating vortices (Fig. 8d) that again increase in spatial unsteadiness (Fig. 9d). However, with a moving ground plane, no clear vortices were now observed (Fig. 9h). Indeed, with the rolling road in operation, the critical blow-away condition will be reached at a higher velocity ratio in comparison with the static ground case due to the nonexistence of the approaching boundary layer. Nevertheless, there is some small evidence of flow disturbance just at the intake lip (Fig. 8h), which may indicate that the diminishing vortices have been blown underneath the intake itself.

2. *Effect of Synchronized Rolling Road on Vortex Strength*

To quantitatively establish the effect of the moving ground, the total nondimensional vortex strength of the vortex system, Γ^*, has been determined for all rolling road configurations. This enables direct comparisons to be made with the static ground results presented in Sec. III. The effect of increasing the ground speed (U_g) synchronized with the tunnel freestream velocity (U_∞) on the total average nondimensional vortex strength is presented in Fig. 11. The static ground configurations for an increasing headwind are also included in the figure for comparison. For low ground speeds

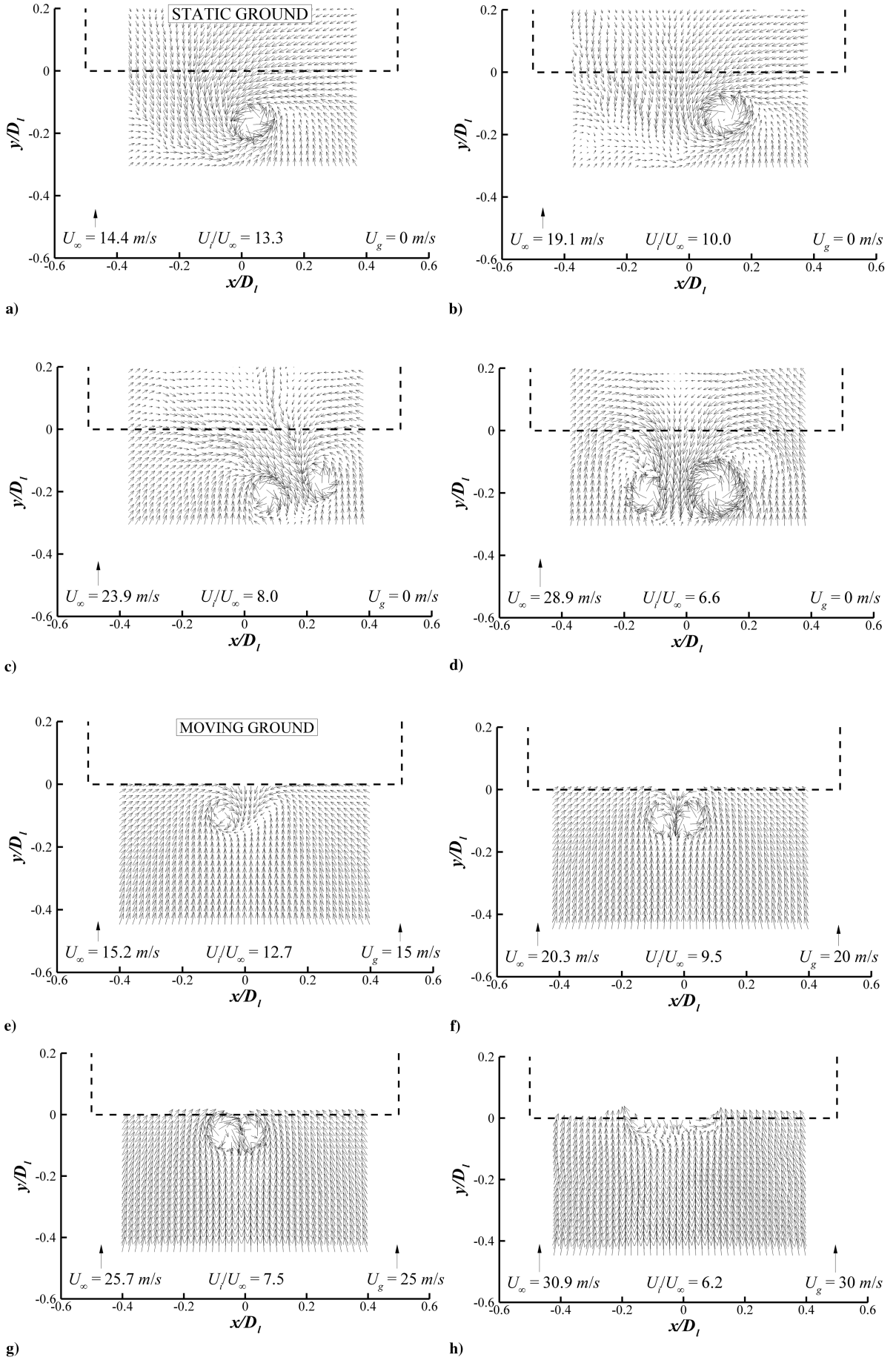

Fig. 8 Example flowfield snapshots of the in-plane velocity vectors for increasing headwind speed comparing a–d) static ground, and e–h) moving ground cases ($h/D_l = 0.25$, $M_t = 0.58$).

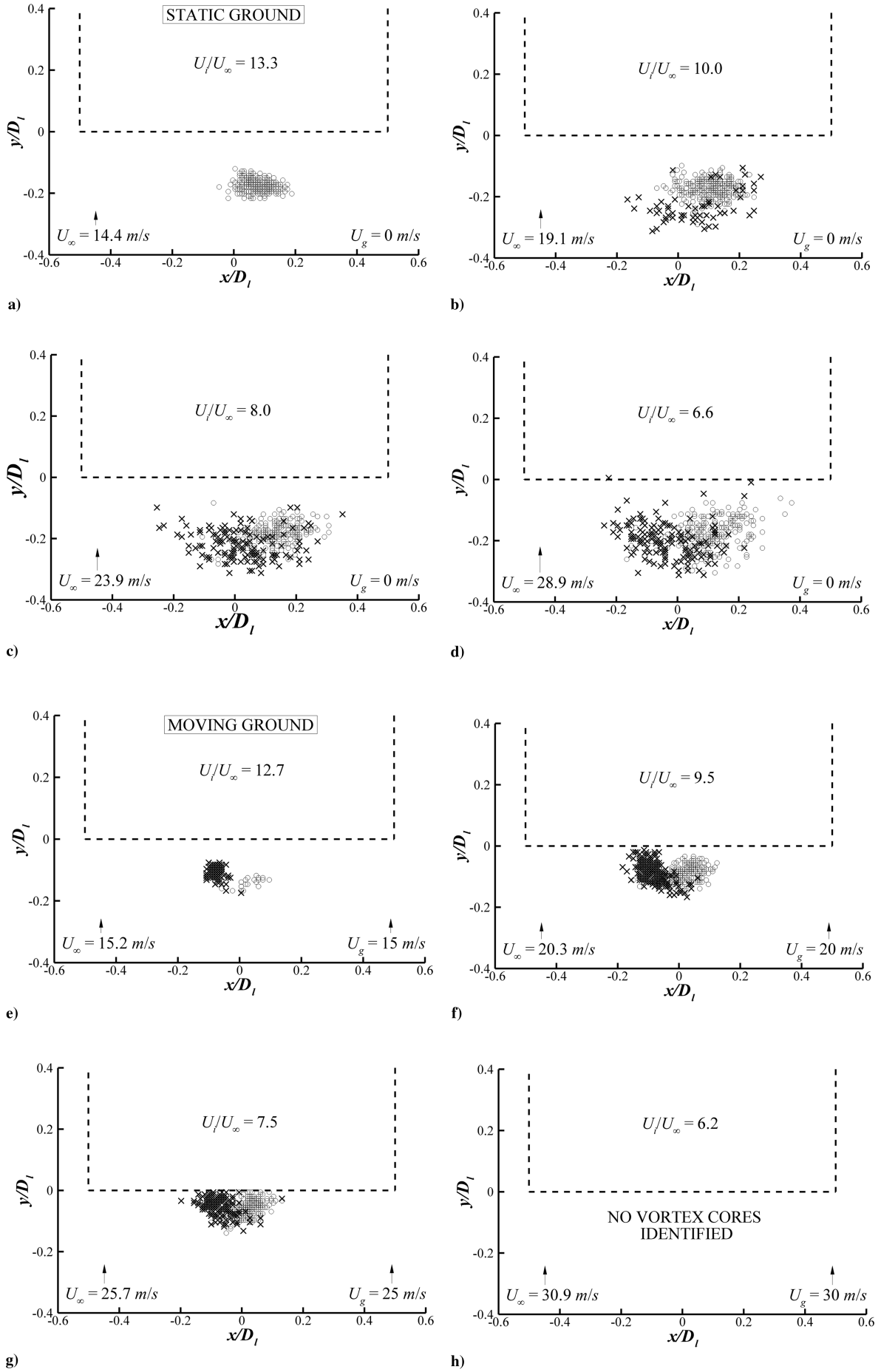

Fig. 9 Locus of vortex core positions over all flowfield snapshots for a–d) static ground, and e–h) rolling ground cases for an increasing headwind ($h/D_l = 0.25$, $M_i = 0.58$) (x: negative vortex; circle: positive vortex).

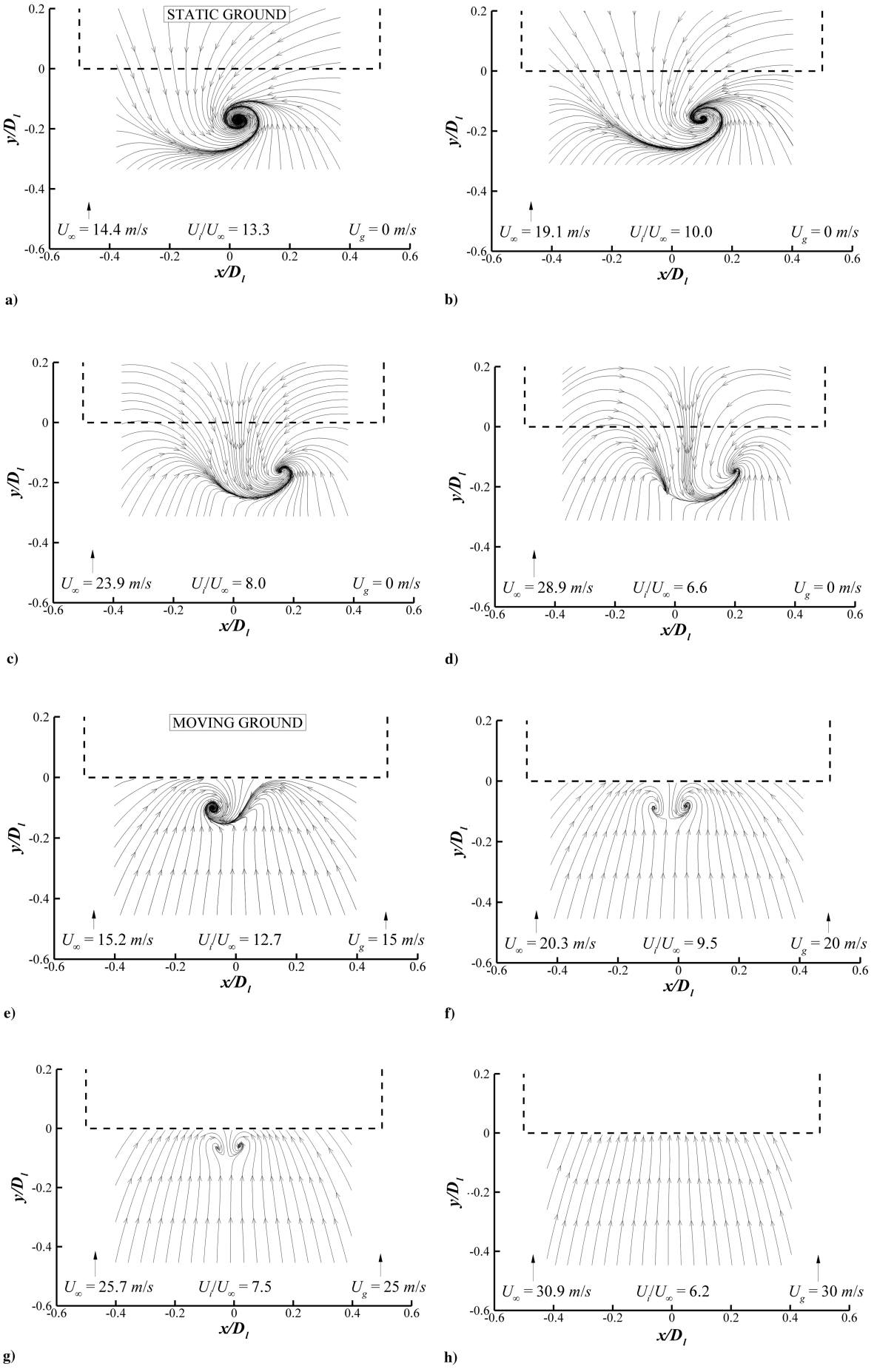

Fig. 10 Time average 2-D bound streamlines for an increasing headwind, U_∞, for a–d) static ground and e–h) moving ground cases ($h/D_l = 0.25$, $\delta^*/D_l = 0.11$, $M_i = 0.58$).

($U_g = 0$–15 m/s), and correspondingly high velocity ratios ($U_i/U_\infty = 12.7 - \infty$), the total vortex strength is almost identical to the corresponding static ground configurations (Fig. 11). Because there is very little approaching boundary-layer vorticity flux, this indicates that the dominant vorticity source, for a static ground ($U_g = 0$ m/s), at intermediate-to-high velocity ratios, is the suction induced vorticity. As U_g increases further and the velocity ratio (U_i/U_∞) reduces, a deviation in the strength from the static road configurations is seen, at this nondimensional height ($h/D_l = 0.25$), when the velocity ratio reaches about 9.5 (A.4, Fig. 11). At this headwind speed, for the static ground plane, the approaching boundary-layer vorticity becomes influential on total vortex strength. With a further increase in the ground speed, U_g, to 25 m/s (A.5, $U_i/U_\infty = 7.5$), there is approximately a 50% reduction in the strength in comparison to the static ground case at the same velocity ratio (Fig. 11). As the ground speed increases further and the velocity ratio, U_i/U_∞, reduces to 6.2, no vortex was detected in the measurement area; therefore, no additional measurements could be taken. Overall, this shows that there is a large reduction in the ground vortex strength and notable differences in the flow structure when comparing a static and a moving ground case.

A small set of PIV measurements were also taken to quantify the effect of ground clearance for the synchronized wind and road velocity configurations. Velocity ratios, U_i/U_∞, of 19.5 and 12.7 were examined (A.2 and A.3) at a nondimensional height, h/D_l, of 0.4. The vortex strength at this higher height-to-diameter ratio is illustrated in Fig. 12 and compared with the static ground cases at the same h/D_l along with the measurements at the datum height of 0.25 (h/D_l). As with the low ground clearance configuration, removing the approaching vorticity source has little effect on the total vortex circulation at relatively high velocity ratios. Because the vortex strength is higher at the larger h/D_l, this indicates that the induced vorticity increases in strength as the ground clearance increases. As discussed in [4], this increase in strength is postulated to be associated with an increased flow emanating from below the intake, as h/D_l is increased. At lower ground clearances the increased proximity to the ground plane restricts the airflow from beneath the nacelle, forcing a larger proportion of mass flow to be ingested from above the intake.

3. In-Duct Total Pressure Survey

In addition to the PIV measurements, an in-duct total pressure survey was also conducted to quantify the flowfield inside the intake duct as well as to support the velocity measurements. To characterize the level of distortion generated by the vortex, the DC_{60} parameter is used, which is defined as follows:

$$DC_{60} = \frac{P_f - P_{60}}{q_f} \tag{4}$$

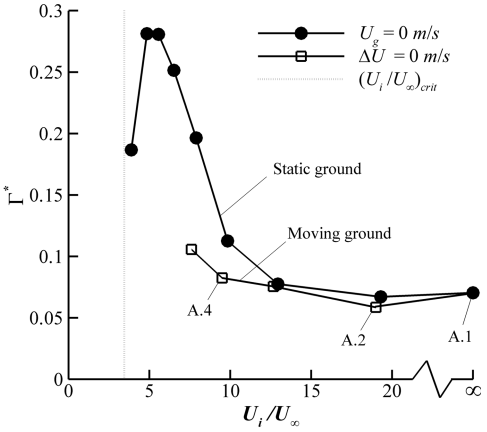

Fig. 11 Average nondimensional vortex strength, Γ*, against velocity ratio, U_i/U_∞, for a moving ground with comparison to a static ground ($h/D_l = 0.25$, $M_i = 0.58$). Note the labels represent the test configurations in Table 1.

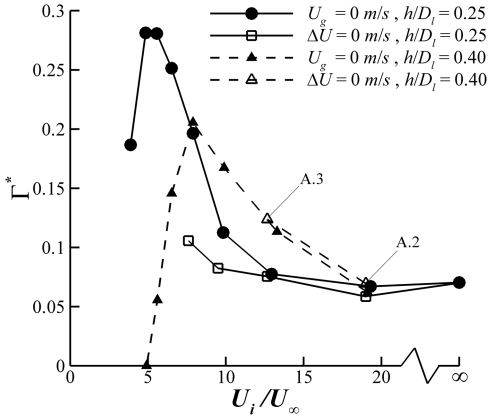

Fig. 12 Average nondimensional vortex strength, Γ*, against velocity ratio, U_i/U_∞, for synchronized moving ground and static ground cases at two nondimensional heights.

Figure 13 compares the DC_{60} trend with increasing headwind speed (reducing velocity ratio, U_i/U_∞) for both static ($U_g = 0$ m/s) and moving ground ($\Delta U = 0$ m/s) cases. In general, the distortion coefficient decreases with increasing ground speed and the concomitant reducing velocity ratio (U_i/U_∞). The trend is comparatively different to the circulation measurements at the PIV plane where the vortex strength remains roughly constant (Fig. 11). The reduction in DC_{60} is associated with the changes to the loss core immediately adjacent to the duct surface (Fig. 6c) gradually diminishing as the velocity ratio reduces. As mentioned earlier, it has been observed in previous work [16] that this localized loss region is due to the interaction of the two vortex loss cores with the intake wall. This interaction will depend on a number of features such as the vortex ingestion location, the vortex strength, and also the separation between the two loss cores. It is clear from the PIV velocity measurements that the vortices move progressively closer together and also closer to the intake highlight plane as the velocity ratio reduces (Fig. 9), which could therefore result in a smaller loss core. In addition, because measurements can only be taken at a finite distance from the wall, measurement resolution close to the duct surface could also be a contributing factor in the DC_{60} trend.

B. Unsynchronized Wind and Road Experiments

In this section, results are presented to simulate an aircraft takeoff for which there is also an approaching headwind velocity. As explained earlier, to simulate the various moving aircraft configurations with a headwind velocity (ΔU), the ground speed is set to match the required intake movement (U_g), and the tunnel wind speed (U_∞) is set to maintain the required additional effective headwind

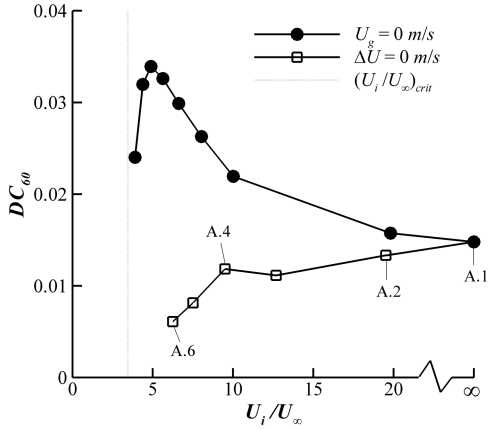

Fig. 13 Fan face distortion for increasing ground speed synchronized with the freestream speed ($\Delta U = 0$ m/s) with comparison to a static ground ($U_g = 0$ m/s) in an increasing headwind ($h/D_l = 0.25$, $M_i = 0.58$).

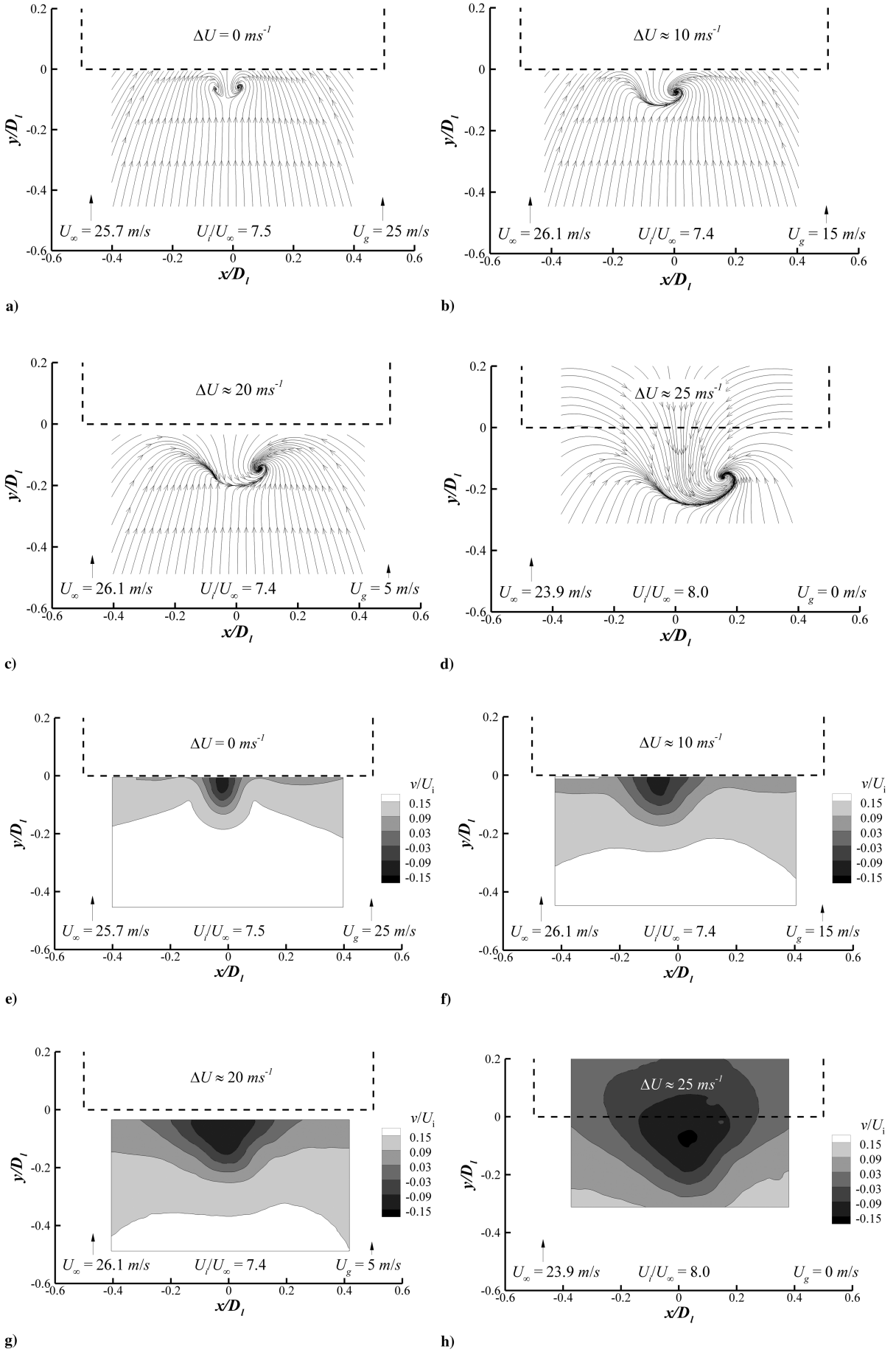

Fig. 14 Effect of ground velocity, U_g, on the time average: a–d) 2-D bound streamlines, and e–h) the nondimensional v-velocity contours at approximately a constant velocity ratio ($h/D_l = 0.25$, $M_i = 0.58$, $U_i/U_\infty \approx 7.5$). Note b and f are configuration C.2, c and g are B.4, and d and h are A.5 (Tables 1 and 2).

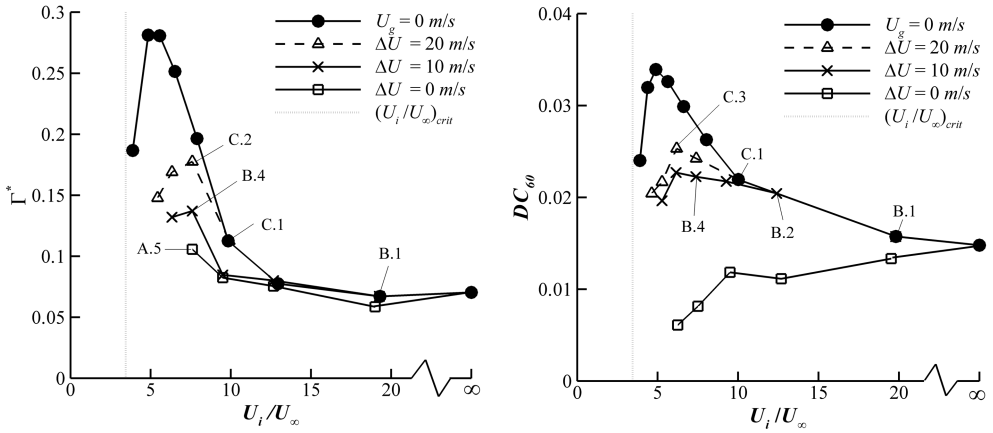

Fig. 15 Effect asynchronous and synchronous rolling road with comparison to the static ground configurations ($h/D_l = 0.25$, $M_i = 0.58$, $\delta^*/D_l = 0.11$): a) nondimensional vortex circulation, Γ^*; and b) the distortion coefficient at the fan face against velocity ratio, U_i/U_∞.

velocity ($U_\infty = \Delta U + U_g$). A range of increasing magnitudes of U_∞ and U_g are examined while keeping ΔU constant. For the unsynchronized experiments two data sets were conducted with ΔU equal to 10 and 20 m/s (Table 2).

The effect of unsynchronizing the ground speed with respect to the tunnel velocity for varying magnitudes of ΔU ranging from zero (i.e., a fully synchronized configuration) to 25 m/s (a static ground configuration), on the time average flowfield is shown in Fig. 14. (Note that Figs. 14a and 14d are the same as Figs. 10g and 10c). This sequence is at a fixed velocity ratio of approximately 7.5 and shows the 2-D bound streamlines (Figs. 14a–14d) as well as the nondimensional v-velocity contours (Figs. 14e–14h). For a synchronized configuration at a velocity ratio of 7.5 (U_i/U_∞), the flowfield has a symmetric vortex topology that is also symmetric relative to the intake axis (Fig. 14a). For this configuration the vortices are relatively steady in space. However, as the ground speed is reduced, at fixed headwind speed, U_∞, the local footprint of the sucked stream tube increases due to the increase in the interaction with the ground plane (Figs. 14a–14d) and the reverse flow emanating from underneath and behind the intake gets progressively stronger (Figs. 14e–14h). In turn, the time-averaged 2-D bound streamlines become increasingly asymmetric (Figs. 14a–14d). The above observations indicate that the asymmetries relating to the ground vortex flowfield for a static ground plane are related to the induced flow emanating from underneath and behind the intake, rather than asymmetries associated with the tunnel flow.

The vortex strength as a function of velocity ratio for all three magnitudes of ΔU is shown in Fig. 15a for the rolling ground plane experiments. The results are also compared to the baseline static ground configurations ($U_g = 0$ m/s). The trends observed are in line with expectations. As the difference between the road and tunnel velocity (ΔU) increases, the vortex gets stronger with vortex formation being observed at increasingly lower velocity ratios (Fig. 15a). The increase in strength of the vortex system is a direct result of the approaching vorticity increasing, as ΔU increases. The reduction in the lowest velocity ratio at which a vortex is observed is due to the average velocity within the sucked stream tube reducing for a given velocity ratio. In turn, the capture stream tube increases for a given U_i/U_∞ and, because vortex formation is dependent on the sucked stream tube interaction with the ground, an ingested vortex system is observed at lower velocity ratios. Similar characteristics are also seen for the distortion coefficient (Fig. 15b). In general, the trends clearly indicate that the higher the ambient headwind during takeoff (i.e., the larger the value of ΔU), the higher the level of strength reached by the vortex system.

V. Conclusions

A study has been conducted to examine the effect of a moving aircraft over a stationary surface on ground vortex formation under headwind conditions. Two types of rolling road experiments have been performed. In the first, the ground and tunnel velocities have been synchronized and, in the second, they have been unsynchronized. In the former case, there is no approaching boundary layer, whereas in the latter there is an approaching vorticity source; however, its strength is lower than the static ground case. All rolling road configurations have been compared to the experiments performed with an intake with a static ground plane in an increasing headwind.

Overall this study has shown the importance of simulating the moving ground plane when considering the characteristics of an intake ground vortex for an aircraft during takeoff. The effects are primarily seen in the low-velocity ratio regime in which large differences are observed between static and moving ground cases in terms of the vortex topology and spatial and temporal unsteadiness, as well as the important vortex strength. In particular, much of the previous ground vortex studies and guidelines have focused on static ground configurations in which the ground vortex strength has now been shown to increase sharply as the velocity ratio reduces before the important blow-away condition is achieved. These latest investigations show that, for a moving aircraft situation, it is overly pessimistic to rely on the static ground database, as the ground vortex formation characteristics are altered and the resulting vortex potency is significantly reduced when the moving ground is taken into account.

Acknowledgments

J. Murphy was funded by an Engineering and Physical Sciences Research Council studentship. The authors would like to thank Rolls-Royce for technical and financial support.

References

[1] Rodert, L. A., and Garrett, F. B., "Ingestion of Foreign Objects into Turbine Engines by Vortices," NACA TN 3330, 1953.

[2] Glenny, D. E., "Ingestion of Debris into Intakes by Vortex Action," National Gas Turbine Establishment Paper 1114, 1968.

[3] Motycka, D. L., "Ground Vortex—Limit to Engine/Reverser Operation," American Society of Mechanical Engineers Paper 75-GT-3, 1975.

[4] Murphy, J. P., "Intake Ground Vortex Aerodynamics," Ph.D. Thesis, Cranfield Univ., Bedford, England, UK, 2008.

[5] Green, J. S., "Forced Response of a Large Civil Fan Assembly," American Society of Mechanical Engineers Paper GT2008-50319, June 2008.

[6] de Siervi, F., Viguier, H. C., and Greitzer, E. M., "Mechanisms of Inlet Vortex Formation," *Journal of Fluid Mechanics*, Vol. 124, 1982, pp. 173–207. doi:10.1017/S0022112082002456

[7] Shin, H. W., Cheng, W. K., and Greitzer, E. M., "Inlet Vortex Formation Due to Ambient Vorticity Intensification," *AIAA Journal*, Vol. 24, No. 4, 1986, pp. 687–689. doi:10.2514/3.9330

[8] Brix, S., Neuwerth, G., and Jacob, D., "The Inlet-Vortex System of Jet Engines Operating Near the Ground," AIAA Paper 2000-3998, 2000.

[9] Dimitriou, I., "Use of a Narrow Belt for Moving Ground Simulation and Its Effect on the Aerodynamic Forces Generated on a Formula-1 Car," MSc Thesis, Cranfield Univ., Bedford, England, UK, 2001.

[10] Jeong, J., and Hussain, F., "On the Identification of a Vortex," *Journal of Fluid Mechanics*, Vol. 285, 1995, pp. 69–94. doi:10.1017/S0022112095000462

[11] Burley, C. L., Brooks, T. F., and Van der Wall, B., "Rotor Wake Vortex Definition—Initial Evaluation of 3-C PIV Results of the Hart-II Study," Royal Aeronautical Society Paper 50, Sept. 2002.

[12] Taylor, J. R., "An Introduction to Error Analysis: The Study of Uncertainties in Physical Measurements," Univ. Science Books, Herndon, VA, 1982.

[13] Raffel, M., Willert, C., and Kompenhans, J., *Particle Image Velocimetry: A Practical Guide*, Springer–Verlag, Berlin, 1998.

[14] Petracci, A., Van Doorne, C. W. H., and Westerweel, J., "Analysis of Stereoscopic PIV Measurements using Synthetic Images," *Particle Image Velocimetry: Recent Improvements*, Springer, Berlin, 2004.

[15] Prasad, A. K., "Stereoscopic Particle Image Velocimetry," *Experiments in Fluids*, Vol. 29, No. 2, 2000, pp. 103–116. doi:10.1007/s003480000143

[16] Zantopp, S., "Jet Engine Ground Vortex Studies," MSc Thesis, Cranfield Univ., Bedford, England, UK, 2008.

F. Coton
Associate Editor